PHYSICAL REVIEW D VOLUME 37, NUMBER 5 1 MARCH 1988

Axigluon production in hadronic collisions

Jonathan Bagger and Carl Schmidt
Lyman Laboratory of Physics, Harvard University, Cambridge, Massachusetts 02138

Stephen King*
Department of Physics, Boston University, Boston, Massachusetts 02215

(Received 8 September 1987)

Recently proposed chiral-color models predict the existence of a massive color octet of vector bosons, the axigluon. In this paper we investigate axigluon production in hadronic collisions. We compute the single-jet inclusive cross section and the two-jet invariant-mass distribution for the CERN collider, the Fermilab Tevatron, and the Superconducting Super Collider. We use CERN data to exclude axigluon masses between 125 and 275 GeV, subject to a mild constraint on the width.

I. INTRODUCTION

According to the current paradigm of particle physics, the low-energy world is described by an $SU(3)\times SU(2)\times U(1)$ gauge theory, spontaneously broken to $SU(3)\times U(1)$ near the Fermi scale $M_F \sim 250$ GeV. There may be other gauge symmetries above this scale, but it is commonly accepted that $SU(3)\times SU(2)\times U(1)$ is the full gauge group at M_F.

What evidence is there for this? Certainly, with the recent discovery of the W and the Z, the electroweak sector is well described by an $SU(2)\times U(1)$ gauge theory. It is less obvious, however, that the hadronic sector is completely described by color SU(3). At low energies QCD appears to work, but at higher energies there might be more to the story. This possibility motivated the introduction of chiral color as an alternative to pure QCD (Refs. 1 and 2).

The chiral color group is $SU(3)_L\times SU(3)_R$, which breaks to diagonal SU(3) at some scale, leaving standard QCD at low energies. There are many different implementations of chiral color,[2] and all require new particles in varying representations of the gauge groups. The most important model-independent prediction of chiral color is a massive color octet of gauge bosons, the axigluon.

In this paper we investigate the effects of axigluons in hadronic collisions.[3] We consider an axigluon of mass M_A and width Γ_A with axial-vector couplings to the standard quarks. Strong parity requires $g_L = g_R$, which in turn forces the axigluon coupling α_A to equal the QCD coupling α_s. The mass M_A is a free parameter that we take as low as 20 GeV. The width is given by

$$\Gamma_A = \frac{N\alpha_s M_A}{6} , \tag{1.1}$$

where N counts the number of open decay channels. Labeling the fermions by their representations $[SU(3)_L, SU(3)_R]$, we normalize N so that a Dirac quark $[(3,1)+(1,\bar{3})]$ contributes $\Delta N = 1$. With this convention,[4] a Dirac quix $[(\bar{6},1)+(1,6)]$ contributes $\Delta N = 5$, while a dichromatic Weyl fermion $[\bar{3},3]$ contributes $\Delta N = 3$. The value of N ranges from 5 for the known quarks up to 18 for all the particles of the model labeled Mark V in Ref. 2.

In the remainder of this paper we analyze axigluon production at hadronic colliders. We parametrize the axigluons by their mass and width. In Sec. II we present the relevant subprocess cross sections. We compute all two-body scattering processes, including those with one or two axigluons in the final state. In Sec. III we investigate axigluon resonance effects in the single-jet inclusive cross section and in the two-jet invariant-mass distribution. We evaluate our results at energies characteristic of the CERN $p\bar{p}$ collider, the Fermilab Tevatron, and the Superconducting Super Collider (SSC). In Sec. IV we compare our results to the single-jet inclusive cross section measured at the CERN collider. We take smearing corrections into account, and rule out axigluon masses between 125 and 275 GeV, subject to a mild constraint on the width. Section V contains a summary of our results.

II. SUBPROCESS CROSS SECTIONS

In this section we compute the required subprocess cross sections. We group them according to the composition of their final states. Subprocesses with no final-state axigluons are presented in Sec. II A. Those with one or two axigluons are given in Secs. II B and II C.

Before we proceed, we need the relevant Feynman rules. These are shown in Fig. 1, with axigluons indicat-

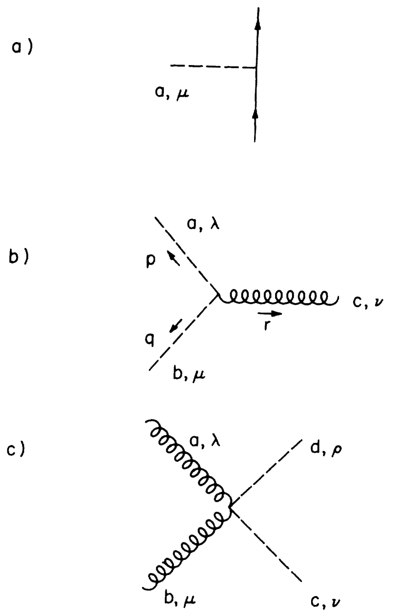

FIG. 1. Feynmann vertices involving axigluons: (a) qqA, $-ig_s\gamma_\mu(T_L^a-T_R^a)$; (b) gAA, $-gf^{abc}[g_{\mu\nu}(r_\lambda-q_\lambda)+g_{\mu\lambda}(q_\nu-p_\nu)+g_{\lambda\nu}(p_\mu-r_\mu)]$; and (c) $ggAA$, $-ig^2[f^{abe}f^{cde}(g_{\lambda\nu}g_{\mu\rho}-g_{\mu\nu}g_{\lambda\rho})+f^{ace}f^{bde}(g_{\lambda\mu}g_{\nu\rho}-g_{\lambda\rho}g_{\mu\nu})+f^{ade}f^{bce}(g_{\lambda\mu}g_{\nu\rho}-g_{\lambda\nu}g_{\mu\rho})]$.

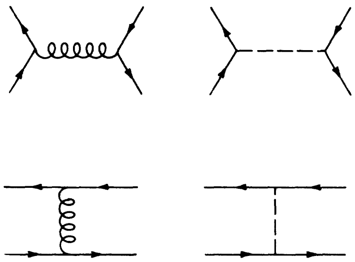

FIG. 2. Quark-antiquark scattering, including gluons and axigluons.

ed by dashed lines. The axigluons couple to fermions by $-ig_s(T_L^a-T_R^a)$, where T_L and T_R are the Weyl-fermion representation matrices of $\mathrm{SU}(3)_L$ and $\mathrm{SU}(3)_R$, respectively. This implies that the coupling to quarks is axial vector. The Feynman rules for the gAA and $ggAA$ vertices are exactly the same as the corresponding three- and four-gluon vertices. Note that because of parity there are no gluon-axigluon vertices with an odd number of axigluons.

A. No-axigluon final states

The two-body scattering processes with no axigluons in the final state are essentially the same as those of lowest-order QCD (Ref. 5). The only difference is that virtual axigluons can be exchanged in intermediate states.

The first process we consider is quark-antiquark scattering, with identical flavors in the initial and final states. This gives rise to the diagrams shown in Fig. 2 and to the following subprocess cross section:

$$\hat\sigma(q_i\bar q_i\to q_i\bar q_i)=\frac{4\alpha_s^2}{9\hat s}\left[(\hat s^2+\hat u^2)\left[\frac{1}{\hat t^2}+\frac{1}{|\hat t_A|^2}\right]+(\hat t^2+\hat u^2)\left[\frac{1}{\hat s^2}+\frac{1}{|\hat s_A|^2}\right]\right.$$
$$-\frac{2}{3}\hat u^2\left[\frac{1}{\hat s\hat t}+\frac{(\hat t-M_A^2)(\hat s-M_A^2)+M_A^2\Gamma_A^2}{|\hat s_A|^2|\hat t_A|^2}\right]$$
$$\left.+\frac{2(\hat t-M_A^2)}{\hat t\,|\hat t_A|^2}(\hat u^2-\hat s^2)+\frac{2(\hat s-M_A^2)}{\hat s\,|\hat s_A|^2}(\hat u^2-\hat t^2)-\frac{2}{3}\hat u^2\left[\frac{\hat s-M_A^2}{\hat t\,|\hat s_A|^2}+\frac{\hat t-M_A^2}{\hat s\,|\hat t_A|^2}\right]\right]. \tag{2.1}$$

The cross section $\hat\sigma$ is defined to be $(\hat s/\pi)d\hat\sigma/d\hat t$. The variables $\hat s$, $\hat t$, and $\hat u$ are the Mandelstam invariants for the interacting partons, where $\hat s=(p_1+p_2)^2$, $\hat t=(p_1-p_3)^2$, and $\hat u=(p_1-p_4)^2$ for the subprocess $\hat\sigma(12\to34)$. We also have defined $\hat t_A=\hat t-M_A^2+iM_A\Gamma_A$ and $\hat s_A=\hat s-M_A^2+iM_A\Gamma_A$. In this formula and in those that follow, all particles except the axigluon are taken to be massless.

Equation (2.1) can be used to find the cross section for quark-antiquark scattering, with different flavors in the initial and final states. One simply drops the t-channel contributions to find

$$\hat\sigma(q_i\bar q_i\to q_j\bar q_j)=\frac{4\alpha_s^2}{9\hat s}\left[(\hat t^2+\hat u^2)\left[\frac{1}{\hat s^2}+\frac{1}{|\hat s_A|^2}\right]+\frac{2(\hat s-M_A^2)}{\hat s\,|\hat s_A|^2}(\hat u^2-\hat t^2)\right]. \tag{2.2}$$

Final states with exotic particle-antiparticle pairs are described by Eq. (2.2), multiplied by the factor ΔN introduced in Sec. I.

The cross section for same-flavor quark-quark or antiquark-antiquark scattering can be obtained from Eq. (2.1) using the crossing symmetry ($\hat t\to\hat u$, $\hat u\to\hat s$, $\hat s\to\hat t$):

$$\hat\sigma(q_iq_i(\bar q_i\bar q_i)\to q_iq_i(\bar q_i\bar q_i))=\frac{4\alpha_s^2}{9\hat s}\left[(\hat t^{\,2}+\hat s^{\,2})\left[\frac{1}{\hat u^{\,2}}+\frac{1}{|\hat u_A|^2}\right]+(\hat u^{\,2}+\hat s^{\,2})\left[\frac{1}{\hat t^{\,2}}+\frac{1}{|\hat t_A|^2}\right]\right.$$
$$-\frac{2}{3}\hat s^{\,2}\left[\frac{1}{\hat t\hat u}+\frac{(\hat u-M_A^2)(\hat t-M_A^2)+M_A^2\Gamma_A^2}{|\hat t_A|^2|\hat u_A|^2}\right]$$
$$+\frac{2(\hat u-M_A^2)}{\hat u|\hat u_A|^2}(\hat s^{\,2}-\hat t^{\,2})+\frac{2(\hat t-M_A^2)}{\hat t|\hat t_A|^2}(\hat s^{\,2}-\hat u^{\,2})$$
$$\left.-\frac{2}{3}\hat s^{\,2}\left[\frac{\hat t-M_A^2}{\hat u|\hat t_A|^2}+\frac{\hat u-M_A^2}{\hat t|\hat u_A|^2}\right]\right]\,. \tag{2.3}$$

Similarly, the cross section for scattering (anti)quarks of different flavors can be obtained using ($\hat t\to\hat u$, $\hat u\to\hat s$, $\hat s\to\hat t$), this time applied to Eq. (2.2):

$$\hat\sigma(q_iq_j(\bar q_i\bar q_j)\to q_iq_j(\bar q_i\bar q_j))=\frac{4\alpha_s^2}{9\hat s}\left[(\hat u^{\,2}+\hat s^{\,2})\left[\frac{1}{\hat t^{\,2}}+\frac{1}{|\hat t_A|^2}\right]+\frac{2(\hat t-M_A^2)}{\hat t|\hat t_A|^2}(\hat s^{\,2}-\hat u^{\,2})\right]\,. \tag{2.4}$$

Finally, the cross section for scattering quarks and antiquarks of different flavors is obtained from Eq. (2.2) by the substitution ($\hat t\to\hat s$, $\hat s\to\hat t$, $\hat u\to\hat u$):

$$\hat\sigma(q_i\bar q_j\to q_i\bar q_j)=\frac{4\alpha_s^2}{9\hat s}\left[(\hat s^{\,2}+\hat u^{\,2})\left[\frac{1}{\hat t^{\,2}}+\frac{1}{|\hat t_A|^2}\right]\right.$$
$$\left.+\frac{2(\hat t-M_A^2)}{\hat t|\hat t_A|^2}(\hat u^{\,2}-\hat s^{\,2})\right]\,. \tag{2.5}$$

All other cross sections are the same as ordinary QCD (Ref. 5).

B. One-axigluon final states

We now compute the subprocess cross sections with one or two axigluons in the final state. The Feynman diagrams for one-axigluon processes are given in Fig. 3.

The cross section for (anti)quark-gluon scattering into (anti)quark-axigluon is given by

$$\hat\sigma(q_ig(\bar q_ig)\to q_iA(\bar q_iA))=\frac{\alpha_s^2}{\hat s}(\hat s^{\,2}+\hat u^{\,2}+2\hat tM_A^2)$$
$$\times\left[\frac{1}{(\hat t-M_A^2)^2}-\frac{4}{9\hat s\hat u}\right]\,. \tag{2.6}$$

The cross section for quark-antiquark scattering into gluon-axigluon is obtained from Eq. (2.6) by crossing ($\hat t\to\hat s$, $\hat s\to\hat t$, $\hat u\to\hat u$):

$$\hat\sigma(q_i\bar q_i\to gA)=\frac{8\alpha_s^2}{3\hat s}(\hat t^{\,2}+\hat u^{\,2}+2\hat sM_A^2)$$
$$\times\left[\frac{4}{9\hat t\hat u}-\frac{1}{(\hat s-M_A^2)^2}\right]\,. \tag{2.7}$$

The factor $\frac{8}{3}$ comes from averaging over colors.

Note that in the limit $M_A\to0$, Eqs. (2.6) and (2.7) reduce to the standard cross sections for ordinary gluon production. This can be understood by noting that the axial-vector nature of the axigluon has no effect on these amplitudes—the γ_5 matrices cancel. Furthermore, the Goldstone bosons that make up the longitudinal part of the axigluon are not produced through these diagrams in the limit that the quarks are massless. Only transverse axigluons are produced, with the same cross section as ordinary gluons.

C. Two-axigluon final states

The Feynman diagrams for two-axigluon final states are shown in Figs. 4 and 5. The cross section describing quark-antiquark scattering into two axigluons is given by

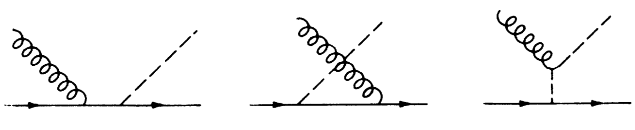

FIG. 3. One-axigluon final-state diagrams.

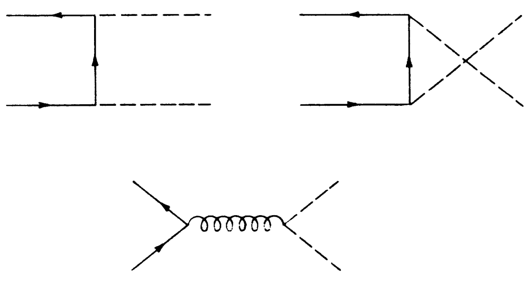

FIG. 4. Two-axigluon final-state diagrams: $q_i\bar q_i\to AA$.

$$\hat{\sigma}(q_i\bar{q}_i \to AA) = \frac{8\alpha_s^2}{3\hat{s}}\left[(\hat{t}^{\,2}+\hat{u}^{\,2})\left[\frac{4}{9\hat{t}\,\hat{u}} - \frac{1}{\hat{s}^{\,2}}\right] + \frac{\hat{u}\,\hat{t}}{\hat{s}^{\,2}} + \frac{2M_A^2}{9}\left[\frac{\hat{u}-2M_A^2}{\hat{u}^{\,2}} + \frac{\hat{t}-2M_A^2}{\hat{t}^{\,2}} - \frac{2M_A^2}{\hat{u}\,\hat{t}}\right]\right.$$
$$\left. - \frac{M_A^2}{2}\left[\frac{\hat{s}-2M_A^2}{\hat{s}^{\,2}} + \frac{\hat{u}^{\,2}+\hat{t}^{\,2}}{\hat{u}\,\hat{s}\,\hat{t}}\right] - \frac{5M_A^2}{2}\left[\frac{1}{\hat{u}}+\frac{1}{\hat{s}}+\frac{1}{\hat{t}}\right]\right] . \tag{2.8}$$

The longitudinal part of the axigluon does not decouple as $M_A \to 0$. The additional term $8\alpha_s^2\hat{u}\,\hat{t}/3\hat{s}^{\,3}$ is precisely the cross section for the production of an octet of real scalars through a virtual gluon.

The remaining subprocess is the scattering of two gluons into two axigluons. The cross section may be expressed as

$$\hat{\sigma}(gg \to AA) = \frac{9\alpha_s^2}{2\hat{s}}\left[\frac{7}{2} - \frac{3}{2}\frac{(\hat{u}-M_A^2)(\hat{t}-M_A^2)}{\hat{s}^{\,2}} - \frac{\hat{s}(\hat{u}-M_A^2)}{(\hat{t}-M_A^2)^2} - \frac{\hat{s}(\hat{t}-M_A^2)}{(\hat{u}-M_A^2)^2}\right.$$
$$\left. + \frac{3M_A^2}{\hat{s}}\left[1-\frac{\hat{s}M_A^2}{(\hat{u}-M_A^2)(\hat{t}-M_A^2)}\right]\left[1-\frac{\hat{s}^{\,2}}{(\hat{u}-M_A^2)(\hat{t}-M_A^2)}\right]\right] . \tag{2.9}$$

As before, the longitudinal axigluon does not decouple in the massless limit. The crossing symmetry ($u \leftrightarrow t$) is manifest in Eqs. (2.8) and (2.9).

III. AXIGLUON SIGNATURES

Now that we have the subprocess cross sections, we are ready to study axigluon effects at hadronic colliders. We consider two separate signatures: the appearance of a peak or some other large deviation from QCD in the single-jet inclusive cross section, and the appearance of an axigluon resonance in the two-jet invariant-mass plot. We evaluate our results at three characteristic center-of-mass energies: 630 GeV, for the CERN $p\bar{p}$ collider; 2 TeV, for the Fermilab Tevatron; and 40 TeV, for the proposed Superconducting Super Collider.

The single-jet and two-jet signatures depend on the resonant production of s-channel axigluons. The production cross section is easily computed to be

$$\sigma = \int \frac{16\pi^2\alpha_s}{9s}\sum_i [f_{q_i}^{(a)}(x_a,M_A^2)f_{\bar{q}_i}^{(b)}(x_b,M_A^2) + f_{\bar{q}_i}^{(a)}(x_a,M_A^2)f_{q_i}^{(b)}(x_b,M_A^2)]dy \ , \tag{3.1}$$

where the sum is over quark flavors; the integral is over the rapidity of the axigluon, $-\ln(\sqrt{s}/M_A) \le y \le \ln(\sqrt{s}/M_A)$; and $f_i^{(a)}(x_a,M_A^2)$ is the structure function for parton i coming from hadron a with momentum fraction x_a. In this and in all our numerical work we use the structure functions of Eichten, Hinchliffe, Lane, and Quigg[5] with $\Lambda_{\rm QCD}=0.20$ GeV. We have checked that our results do not depend strongly on this choice.

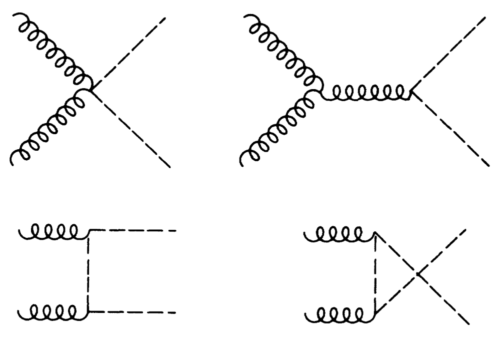

FIG. 5. Two-axigluon final-state diagrams: $gg \to AA$.

In Fig. 6 we present the resonance production cross sections as a function of mass, for $p\bar{p}$ interactions at $\sqrt{s}=630$ GeV and 2 TeV, and for pp interactions at 40 TeV. We see that axigluon masses of 200 GeV correspond to cross sections ranging from 5 nb at $\sqrt{s}=630$ GeV to 250 nb at $\sqrt{s}=40$ TeV. The cross section drops to 0.01 nb for 1-TeV axigluons in 2-TeV collisions. Note that at 630 GeV the cross section for a 100-GeV axigluon is fifty times larger than that for a W or Z boson. The large cross section is the result of a color factor and the strong QCD coupling.

Whether these axigluons can be seen, however, depends on the magnitude of the QCD background. In the following sections we examine axigluon production in relation to this background.

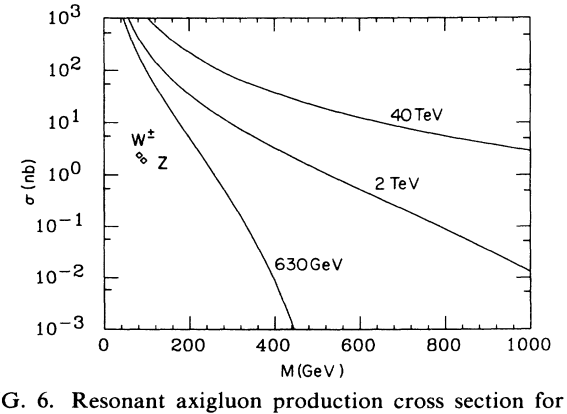

FIG. 6. Resonant axigluon production cross section for $p\bar{p}$ scattering at $\sqrt{s}=630$ GeV and 2 TeV, and for pp interactions at 40 TeV, as a function of mass.

A. Single-jet inclusive cross section

In a given energy region, the first place to look for axigluons is in the single-jet inclusive cross section. To lowest order, the single-jet cross section is given by

$$\left.\frac{d\sigma}{dp_\perp dy}\right|_{y=0} = \int \frac{2\pi\tau}{\hat{s}} p_\perp \sum_{ij} f_i^{(a)}(x_a,Q^2) f_j^{(b)}(x_b,Q^2) \times \hat{\sigma}_{ij}(\hat{s},\hat{t},\hat{u})\,dy_2 , \qquad (3.2)$$

where $y=0$ indicates that the observed jet is perpendicular to the beam axis. In this equation $\tau = x_a x_b$, and $\hat{\sigma}_{ij}$ is the inclusive subprocess cross section for initial partons i and j scattering into all distinguishable final-state configurations. The integral is over the rapidity y_2 of the second jet. The limits of integration are given by $-\ln[(\sqrt{s}-m_{1\perp})/m_{2\perp}] \le y_2 \le \ln[(\sqrt{s}-m_{1\perp})/m_{2\perp}]$, where $m_{i\perp}^2 = p_\perp^2 + m_i^2$, m_1 is the mass of the observed jet, and m_2 is the mass of the recoil jet. As before, we take $\Lambda_{\rm QCD} = 0.20$ GeV in the four-flavor regime. We evaluate the structure functions and α_s at $Q^2 = p_\perp^2$ for no-axigluon final states, and $Q^2 = p_\perp^2 + M_A^2$ for one- and two-axigluon final states.

In Fig. 7 we present a plot of $d\sigma/dp_\perp dy\,|_{y=0}$ for $p\bar{p}$ scattering at 630 GeV. We show the QCD cross section, plus cross sections with axigluons of masses 100, 150, 200, 250, and 300 GeV for $N=5$ open quark channels. Figure 7 exhibits the exponentially falling cross section of the QCD background. Superimposed on the background, for each choice of mass, is a peak at approximately $M_A/2$. This is the Jacobian peak arising from resonant axigluons in the s channel. Note that the axigluon curves settle back towards the QCD background[6] for $p_\perp \gg M_A/2$.

Figure 7 shows that the Jacobian peaks are more pronounced for larger axigluon masses. This can be easily understood from Figs. 8 and 9, where we present sample cross sections, broken down according to their subprocess contributions. The peaks come from the s-channel resonances of Eqs. (2.1) and (2.2). At low transverse momenta the peaks are hidden by gluonic jets.

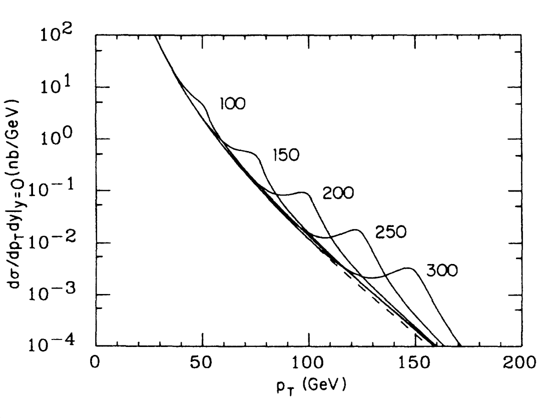

FIG. 7. Single-jet inclusive cross section for $p\bar{p}$ scattering at $\sqrt{s}=630$ GeV. Shown are QCD (dashed curve) and chiral color (solid curve) with axigluons of mass $M_A = 100$, 150, 200, 250, and 300 GeV for $N=5$.

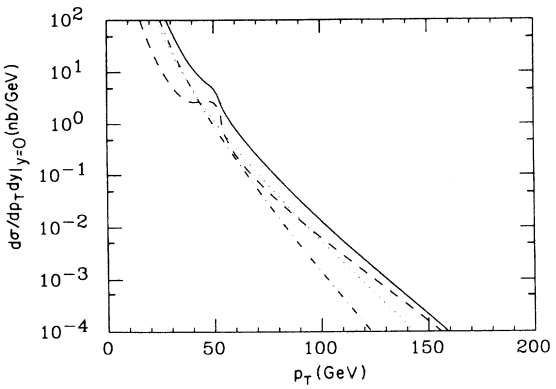

FIG. 8. Single-jet inclusive cross section for $p\bar{p}$ scattering at $\sqrt{s}=630$ GeV for axigluon mass of 100 GeV with $N=5$, subdivided according to initial partons. The subprocesses are gg (dot-dashed curve), gq (dotted curve), qq (dashed curve), and total (solid curve).

Figures 8 and 9 illustrate that the magnitude of the gluonic background is a major factor in determining the relative size of the peaks. This implies that any uncertainties in the gluonic structure function give rise to associated uncertainties in the relative height of the peak over the background.

A second factor contributing to the relative height of the peak over background is the value of the strong coupling α_s. On resonance the cross section is independent of α_s, but off resonance it scales like α_s^2. Therefore, increasing α_s decreases the prominence of the peak. This is seen in Figs. 8 and 9 by the relative size of the resonance in the quark subprocess. At low $p_\perp$, α_s is large, so the peak is small. At high $p_\perp$, on the other hand, α_s is smaller, so the peak is larger. This effect also contributes an overall uncertainty at fixed $p_\perp$. For a typical mass, changing $\Lambda_{\rm QCD}$ from 100 to 300 MeV decreases the signal-to-background ratio by about 20%.

In Fig. 10 we present the single-jet inclusive cross sec-

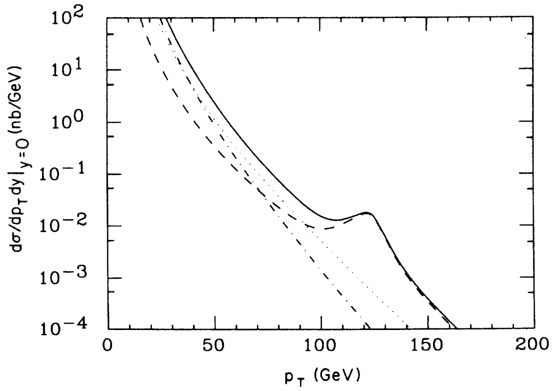

FIG. 9. Single-jet inclusive cross section for $p\bar{p}$ scattering at $\sqrt{s}=630$ GeV for axigluon mass of 250 GeV with $N=5$, subdivided according to initial partons. The subprocesses are gg (dot-dashed curve), gq (dotted curve), qq (dashed curve), and total (solid curve).

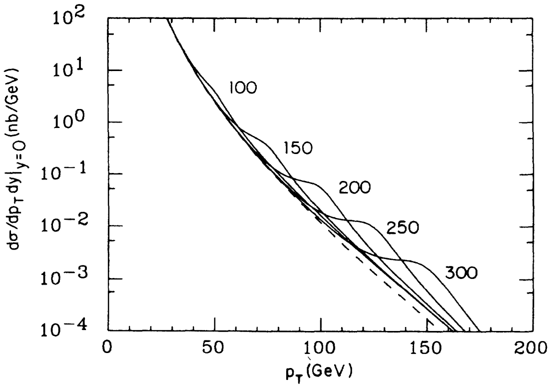

FIG. 10. Single-jet inclusive cross section for $p\bar{p}$ scattering at $\sqrt{s}=630$ GeV. Shown are QCD (dashed curve) and chiral color (solid curve) with axigluons of mass $M_A=100$, 150, 200, 250, and 300 GeV for $N=10$.

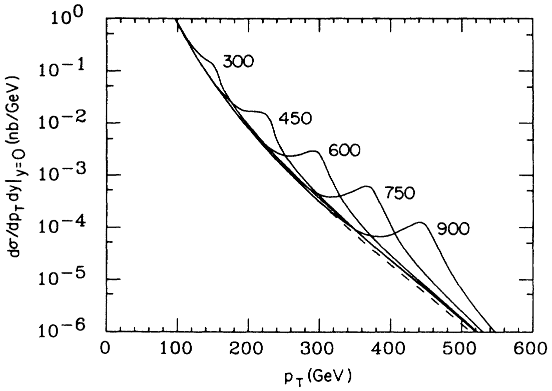

FIG. 11. Single-jet inclusive cross section for $p\bar{p}$ scattering at $\sqrt{s}=2$ TeV. Shown are QCD (dashed curve) and chiral color (solid curve) with axigluons of mass $M_A=300$, 450, 600, 750, and 900 GeV for $N=5$.

tion at $\sqrt{s}=630$ GeV for $N=10$ open quark channels. By comparing Figs. 7 and 10, we see that the Jacobian peaks are less pronounced for larger axigluon widths. Even for $N=10$, however, it is easier to look for axigluons through their Jacobian peaks than through deviations from QCD on the high-$p_\perp$ tail.

For a given width axigluon, a hadronic collider of fixed $\sqrt{s}$ is sensitive to a finite range of mass. The upper limit is set by luminosity: at high $p_\perp$ the cross section becomes too small for the peak to be seen. The lower limit occurs when the peak sinks in a sea of soft gluonic jets. In Sec. IV we will use the data of the UA1 Collaboration[7] to place preliminary bounds on the axigluon mass and width.

Figures 7 and 10 include all final states, including those with axigluons. For the intermediate-mass axigluons considered above, it is not completely correct to sum over the axigluon final states. The problem is that the massive axigluons do not necessarily give rise to simple two-jet events. Here, however, no harm is done, for final-state axigluons of intermediate mass do not contribute significantly to the cross section at any value of $p_\perp$. For example, using the published UA1 integrated luminosity of 258 nb^{-1} (Ref. 7), we estimate that only 20 final-state axigluons of mass 150 GeV and 80 of mass 100 GeV should have been produced at the CERN collider, with transverse momenta greater than 40 GeV.

Although final-state axigluons contribute little to the single-jet inclusive cross section, they may still be important for probing low-axigluon masses. For example, axigluons of mass 100 GeV would produce an excess of three- and four-jet events with unusual topologies. Lighter axigluons may be observed as relatively fat single jets or as part of a three- or four-jet event. We estimate that as many as 10^3 final-state axigluons of mass 50 GeV and 10^4 of mass 20 GeV may have been produced at the CERN collider, with transverse momenta greater than 40 GeV. The direct production of light axigluons is sufficiently large that a detailed study of the CERN data may be able to probe axigluons in this range.

The general features of the single-jet inclusive cross section at the CERN $p\bar{p}$ collider are repeated at the Tevatron. This is seen in Fig. 11, where we plot the cross section at $\sqrt{s}=2$ TeV, for QCD and for axigluon masses of 300, 450, 600, 750, and 900 GeV, taking $N=5$. Comparing Figs. 7 and 11, we see that the cross sections scale simply with energy.

Similar results would hold at 40 TeV if the SSC were a $p\bar{p}$ collider. However, the SSC is a pp machine, so the story is very different. At 40 TeV the proton sea does not contain enough antiquarks to create prominent Jacobian peaks. The Jacobian peaks are so small that finding the axigluon through the single-jet cross section would be difficult.

B. Two-jet invariant-mass cross section

A more sensitive way to search for s-channel resonances is to look for peaks in the two-jet invariant-mass plot. The two-jet invariant-mass cross section is given by

$$\frac{d\sigma}{dM}=\int\int\frac{\pi M\tau}{2\hat{s}\cosh^2 y^*}\sum_{ij}f_i^{(a)}(x_a,Q^2)f_j^{(b)}(x_b,Q^2)\times\hat{\sigma}_{ij}(\hat{s},\hat{t},\hat{u})dy_1dy_2\ , \quad (3.3)$$

where $y^*=(y_1-y_2)/2$; Q^2 is as before; M is the two-jet invariant mass; and the integral is over all jets satisfying the rapidity cut $|y_1|,|y_2|\leq Y$. In our plots we have taken $Y=0.85$.

In Figs. 12 and 13 we present $d\sigma/dM$ for $p\bar{p}$ scattering at center-of-mass energy 630 GeV, for $N=5$ and 10 open quark channels, respectively. Each plot contains pure QCD and chiral color with axigluons of masses 100, 150, 200, 250, and 300 GeV. We do not include axigluons in the final states because such processes do not contribute near the s-channel resonance.

Comparing Figs. 12 and 13, we see a pattern similar to that of Figs. 7 and 10. There is a window of potentially observable masses for a given width axigluon. As the width increases, the resonant peak should become more

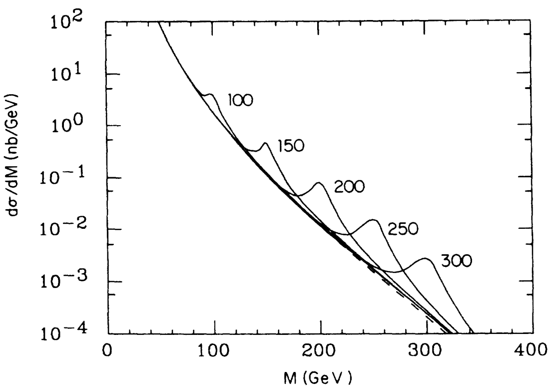

FIG. 12. Two-jet invariant-mass cross section for $p\bar{p}$ scattering at $\sqrt{s}=630$ GeV. Shown are QCD (dashed curve) and chiral color (solid curve) with axigluons of mass $M_A=100$, 150, 200, 250, and 300 GeV for $N=5$.

difficult to reconstruct. As a point of reference, the effects of the W and Z would barely be visible on these plots. Thus, an investigation similar to the UA2 search for W and Z resonances[8] should be able to strongly constrain the axigluon in this energy range.

In Fig. 14 we present the two-jet invariant-mass cross sections for a $p\bar{p}$ collider of energy 2 TeV. We plot QCD and chiral color with axigluon masses of 300, 450, 600, 750, and 900 GeV, and $N=5$. Note the approximate scaling relative to the CERN collider. The peaks are somewhat larger, however, because α_s is smaller.

Figure 15 contains the two-jet invariant-mass plot for pp interactions at 40 TeV. We include QCD and chiral color with axigluon masses of 6, 9, 12, and 15 TeV with $N=5$. As with the single-jet cross section, the signal from pp interactions is much smaller than that from $p\bar{p}$. A careful experiment might be able to separate the two-jet resonances from the background at the SSC.

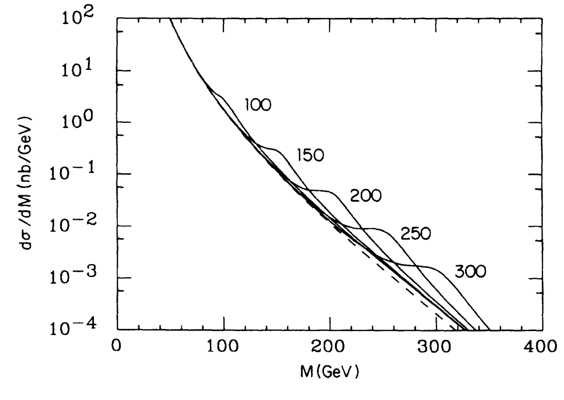

FIG. 13. Two-jet invariant-mass cross section for $p\bar{p}$ scattering at $\sqrt{s}=630$ GeV. Shown are QCD (dashed curve) and chiral color (solid curve) with axigluons of mass $M_A=100$, 150, 200, 250, and 300 GeV for $N=10$.

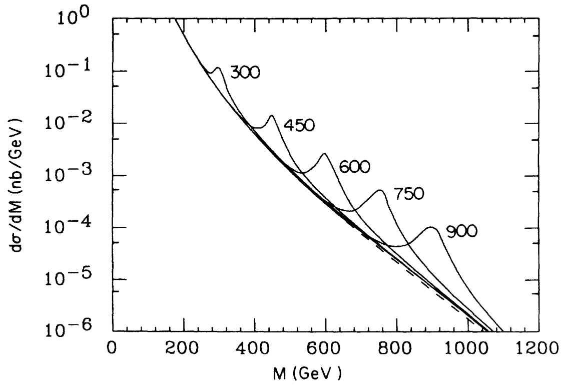

FIG. 14. Two-jet invariant-mass cross section for $p\bar{p}$ scattering at $\sqrt{s}=2$ TeV. Shown are QCD (dashed curve) and chiral color (solid curve) with axigluons of mass $M_A=300$, 450, 600, 750, and 900 GeV for $N=5$.

IV. AXIGLUON BOUNDS FROM COLLIDER DATA

In Sec. III we discussed several signals for axigluon production at hadronic colliders. Most of the signatures require a detailed analysis to separate the signal from background. The single-jet inclusive cross section, however, is sufficiently simple that we can use it here to place preliminary bounds on the axigluon mass and width. As discussed in Sec. III A, the Jacobian peak provides a dramatic signal for axigluons of mass $M_A\sim 2p_\perp$.

In this section we compare our results with recent CERN measurements of the inclusive single-jet cross section. Since the published data extend from $p_\perp=30$ to 150 GeV, the CERN collider probes axigluon masses between 60 and 300 GeV. Even though the single-jet cross section is relatively simple, it is still not completely straightforward to compare theory and experiment. The complication stems from the fact that both UA1 and UA2 correct their raw data for detector resolution and acceptance using a QCD-based Monte Carlo simulation. They present their data in a form that can be directly compared to QCD, but which is not quite sufficient for our purposes.

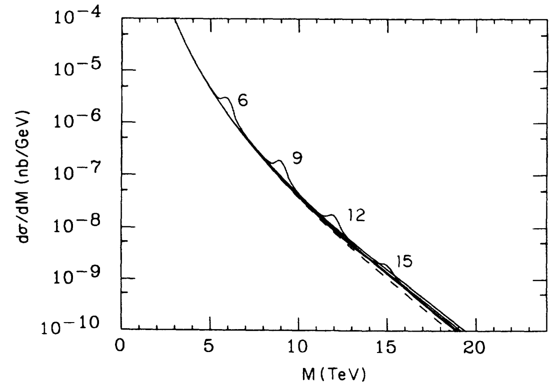

FIG. 15. Two-jet invariant-mass cross section for pp scattering at $\sqrt{s}=40$ TeV. Shown are QCD (dashed curve) and chiral color (solid curve) with axigluons of mass $M_A=6$, 9, 12, and 15 TeV for $N=5$.

To compare our results with the published data, we must follow a two-step procedure. The first step is to smear our curves to account for the effects of finite detector resolution. We do this by convoluting our results with a Gaussian correction function. This relates the true cross section σ_T to the measured cross section σ_M:

$$\sigma_M(p_\perp)=\frac{1}{w\sqrt{2\pi}}\int e^{-(p_\perp-p'_\perp)^2/2w^2}\sigma_T(p'_\perp)dp'_\perp \; , \qquad (4.1)$$

where w is a detector-dependent resolution function. For UA1 (Ref. 9), w has been determined to be $w(p_\perp)=0.05p_\perp+0.53\sqrt{p_\perp}$ ($p_\perp$ in GeV).

The convolution (4.1) smooths out the Jacobian peaks. It also changes the slope of the QCD background. Thus, our second step is to multiply σ_M by a smooth correction factor, designed to restore the QCD baseline.[10] This places our results in a form where they can be directly compared to the published UA1 data. A similar comparison can be made to UA2 data, giving rise to similar results.

Since we are looking for peaks in the data, we must also ask whether the UA1 and UA2 analyses preserved peaks in the raw data. Fortunately, they do, because the total effect of the UA1 and UA2 corrections was to multiply the raw data by a monotonic function of $p_\perp$. For the UA1 analysis this function varies from 0.8 at low $p_\perp$ (30 GeV) to 0.7 at high $p_\perp$ (130 GeV).

In Figs. 16–18 we compare our corrected results to the published UA1 data at $\sqrt{s}=630$ GeV, for $M_A=100$, 150, 200, 250, and 300 GeV, and $N=5$, 10, and 20 open channels.[11] For $N=5$ and 10 the peaks are broader than the analogous unsmeared curves presented in Sec. III A. Note, however, that the effects of the smearing become less important as the width Γ_A becomes larger.

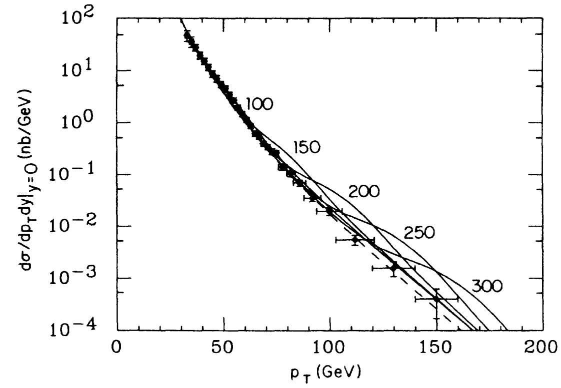

FIG. 17. Single-jet inclusive cross section for $p\bar{p}$ scattering at $\sqrt{s}=630$ GeV, corrected for detector resolution. Shown are UA1 data, QCD (dashed curve), and chiral color (solid curve) with axigluons of mass $M_A=100$, 150, 200, 250, and 300 GeV for $N=10$.

In Fig. 16, with $N=5$, we see that an axigluon of mass $M_A=100$ GeV is allowed, while axigluons in the range $M_A=125$–275 GeV are ruled out. In Fig. 17, with $N=10$, the peaks are less pronounced, but the same mass range is excluded. In Fig. 18, for $N=20$, the peaks are almost completely washed out, but axigluons in the above mass range give rise to a high-$p_\perp$ tail that conflicts with experiment. Thus we see that axigluons of mass $125\leq M_A\leq 275$ GeV are ruled out for $N\leq 20$. For higher N, axigluons are probably excluded because of the rise in the high-$p_\perp$ tail.

V. CONCLUSIONS

In this paper we have investigated axigluon production in hadronic collisions. We have seen that axigluons in the range $125\leq M_A\leq 275$ GeV are in contradiction with data from the CERN collider.

Better bounds can be obtained with a more extensive experimental analysis of the two-jet invariant-mass cross section. We expect that the CERN collider should be able to probe axigluon masses between 100 and 300 GeV, the Tevatron between 300 and 900 GeV, and the SSC be-

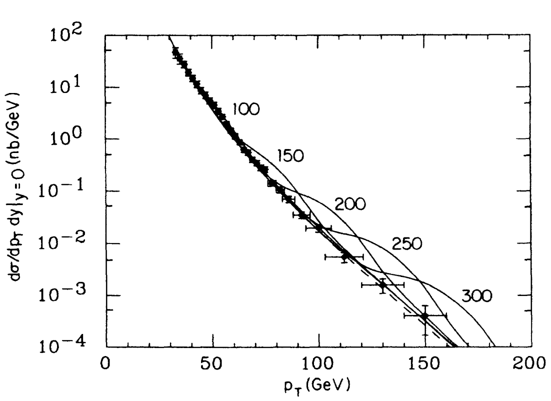

FIG. 16. Single-jet inclusive cross section for $p\bar{p}$ scattering at $\sqrt{s}=630$ GeV, corrected for detector resolution. Shown are UA1 data, QCD (dashed curve), and chiral color (solid curve) with axigluons of mass $M_A=100$, 150, 200, 250, and 300 GeV for $N=5$.

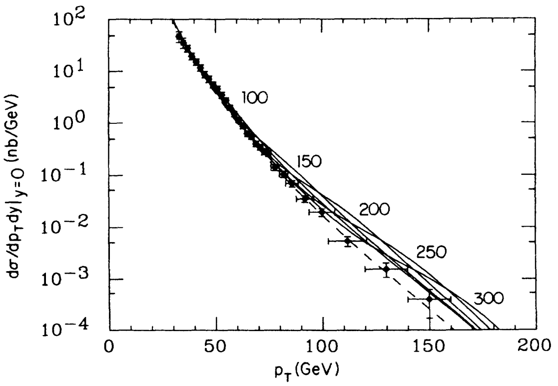

FIG. 18. Single-jet inclusive cross section for $p\bar{p}$ scattering at $\sqrt{s}=630$ GeV, corrected for detector resolution. Shown are UA1 data, QCD (dashed curve), and chiral color (solid curve) with axigluons of mass $M_A=100$, 150, 200, 250, and 300 GeV for $N=20$.

tween 6 and 18 TeV.

Axigluons that are light compared with $\sqrt{s}$ are copiously produced at hadronic colliders. They give rise to single fat jets or closely correlated dijets. A careful analysis of the CERN data might be able to constrain axigluons with masses between 20 and 100 GeV.

Note added in proof. The UA1 Collaboration has recently investigated the two-jet invariant-mass distribution, for four different angular regions. They find good agreement with QCD predictions. For $\Gamma_A = 0.1 M_A$, they reach the preliminary conclusion that axigluon masses are excluded between 110 and 310 GeV, at 95% confidence level.[12]

ACKNOWLEDGMENTS

We would like to thank Ken Lane for several important suggestions; Jim Rohlf and Steve Geer for discussions on the UA1 data; and Paul Frampton and Shelly Glashow for helpful comments. J.B. acknowledges the support of the Alfred P. Sloan Foundation; C.S. was supported by the National Science Foundation Graduate Program; and S.K. is grateful to Asim Yildiz for support. This work was supported in part by National Science Foundation Grants Nos. PHY82-15249 and PHY86-57291, and by Department of Energy Grant No. DE-AC0283ER40118.

---

[*] Present address: Department of Physics, University of Southampton, Southampton SO9 5NH, England.

[1] J. Pati and A. Salam, Phys. Lett. **58B**, 333 (1975); J. Preskill, Nucl. Phys. **B177**, 21 (1981); L. Hall and A. Nelson, Phys. Lett. **153B**, 430 (1985).

[2] P. H. Frampton and S. L. Glashow, Phys. Lett. B **190**, 157 (1987); Phys. Rev. Lett. **58**, 2168 (1987).

[3] Axigluon production in e^+e^- interactions has been considered by T. Rizzo, Phys. Lett. B **197**, 273 (1987).

[4] The general formula for the contribution of each Weyl fermion is $\Delta N = (\dim R) k(L) + (\dim L) k(R)$. In this formula $\dim R, L$ and $k(R,L)$ are the dimension and the index of the fermion representation under $SU(3)_{R,L}$, with the fundamental generators normalized by $\mathrm{tr}\, T^a T^b = \frac{1}{2}\delta^{ab}$.

[5] E. Eichten, I. Hinchliffe, K. Lane, and C. Quigg, Rev. Mod. Phys. **56**, 579 (1984).

[6] The curves approach the QCD background because of the axial nature of the axigluon couplings. If the couplings were vectorial, the curves would run almost four times the QCD background in the limit of large $p_\perp$.

[7] UA1 Collaboration, G. Arnison *et al.*, Phys. Lett. B **172**, 461 (1986).

[8] UA2 Collaboration, R. Ansari *et al.*, Phys. Lett. B **186**, 452 (1987).

[9] We thank Jim Rohlf for providing this information.

[10] We also multiply our results by a constant factor of 1.5, as was done by UA1. The factor of 1.5 is well within the systematic error of QCD calculations because of the ambiguity of the Q^2 scale, the QCD scale parameter, and choice of structure functions.

[11] For $N = 5$ the corresponding widths are 12.4, 17.3, 22.0, and 26.5 GeV. As a percentage of M_A, they are 12.4%, 11.5%, 11.0%, and 10.6%, respectively, where the variation arises from the running of the coupling constant.

[12] S. Geer (private communication).